Ultrafast synthesis of hard carbon anodes for sodium-ion batteries

Yichao Zhen[a], Yang Chen[a,b], Feng Li[a,b], Zhenyu Guo[c] , Zhensheng Hong[a,1], and Maria-Magdalena Titirici[c]

[a]Fujian Provincial Key Laboratory of Quantum Manipulation and New Energy Materials, College of Physics and Energy, Fujian Normal University, Fuzhou, Fujian 350117, China; [b]Fujian Provincial Collaborative Innovation Center for Advanced High-Field Superconducting Materials and Engineering, Fuzhou, 350117, China; and [c]Department of Chemical Engineering, Imperial College London, London, SW7 2AZ, UK

Hard carbons (HCs) are a significantly promising anode material for alkali metal-ion batteries. However, long calcination time and much energy consumption are required for the traditional fabrication way, resulting in an obstacle for high-throughput synthesis and structure regulation of HCs. Herein, we report an emerging sintering method to rapidly fabricate HCs from different carbon precursors at an ultrafast heating rate (300 to 500 °C min^{-1}) under one minute by a multifield-regulated spark plasma sintering (SPS) technology. HCs prepared via the SPS possess significantly fewer defects, lower porosity, and less oxygen content than those pyrolyzed in traditional sintering ways. The molecular dynamics simulations are employed to elucidate the mechanism of the remarkably accelerated pyrolysis from the quickly increased carbon sp^2 content under the multifield effect. As a proof of concept, the SPS-derived HC exhibits an improved initial Coulombic efficiency (88.9%), a larger reversible capacity (299.4 mAh·g^{-1}), and remarkably enhanced rate capacities (136.6 mAh·g^{-1} at 5 A·g^{-1}) than anode materials derived from a traditional route for Na-ion batteries.

sodium-ion batteries | hard carbons | spark plasma sintering | rapid synthesis

Lithium-ion batteries (LIBs) have succeeded greatly in the past decades; however, they are being challenged by the scarcity of lithium-based resources and uneven geographical distribution with the soaring demands in the electric vehicles market and grid-scale energy storage (1, 2). In this context, it is widely accepted that Na-ion batteries (SIBs) are promising alternatives to LIBs, especially in the energy storage grid due to low cost, abundant and environmentally friendly sodium-based resources, and facile and rapid replication from LIBs regarding industrial and commercial processes (2–6). Graphite, a predominant anode material for LIBs, unfortunately, delivers a low capacity (<20 mAh·g^{-1}) in a Na-ion battery using ester electrolytes forming graphite intercalation compounds NaC$_{64}$ rather than thermodynamically unstable NaC$_6$ (7–9). Whereas, hard carbons (HCs) of wider graphene layers, abundant micropores, and rich defects have become one of the most promising candidates as anodes for SIBs, delivering high capacities (250 to 350 mAh·g^{-1}) and low plateau voltage (~0.1 V versus Na/Na$^+$) by integrating Na-ion storage mechanisms of absorption, insertion, and pore-filling (10–13). HCs are suitable for LIBs and K-ion batteries and have decent capacities (14).

HCs were typically prepared through direct sintering, microwave irradiation, or hydrothermal carbonization preprocessing of carbon precursors including common sugars, biomass, or polymer followed by a solid-state sintering process (15–23). HC is generally formed at a temperature between 1,000 and 1,600 °C for several hours in a tubular furnace (TF), and the pyrolysis process plays an essential role in regulating the HC microstructure. A low heating rate (e.g., 0.5 °C min^{-1}) was reported as required to fabricate HC with few defects and low porosity beneficial for high reversible capacity and cycling stability (24). Hence, long calcination time and much energy

consumption are inevitable for traditionally synthesizing HCs. Yet, few reports document sintering technologies of HCs, which also limits high-throughput fabrication and structure regulation of HCs.

Joule heating has been reported as a promising and emerging approach to the flash synthesis of materials through the regulation of an external electric field (25–27). Inspired by this thought, rapid synthesis of HC materials in minutes has been developed through a spark plasma sintering (SPS) technology. SPS is a field-assisted sintering process combining plasma activation, hot pressing, and resistance heating (Fig. 1 A and B show the schematic diagram of our SPS system and the annealing mechanism). Due to the synergy between a high temperature and high pressure, SPS is performed at a hot pressing situation and ultimately can be categorized as a rapid, energy-efficient, and sustainable sintering route (28, 29). Typically, the powder sample is put into a circular graphite tank, and the graphite plate is used as a substrate. The top and bottom graphite plates have the same temperature as the sample because both of them are next to the temperature sensor. Such technology is greatly applicable to fabricate dense materials (29), but it has not been reported in fabricating HC materials. Herein, we report HCs derived from different carbon precursors can be rapidly synthesized via the SPS with few defects, less oxygen content, and enhanced electronic conductivity compared with the samples from the traditional sintering way, leading to enhanced Na-ion storage performance.

Significance

Hard carbon (HC) is one of the most promising anode materials for alkali metal-ion batteries, which is generally prepared by annealing in a tubular furnace with a low heating rate and long duration at a target temperature. Herein, we report an innovating sintering method to quickly fabricate HC even within one minute and ultrafast heating rate by multifield-regulated spark plasma sintering (SPS) technology. This is a universal way to the rapid preparation of various HCs from different carbon precursors. Notably, HCs prepared from SPS possess significantly lower oxygen contents and higher electronic conductivity than the traditional sintering way due to the remarkably accelerated pyrolysis reaction, leading to excellent electrochemical Na-ion storage performance.
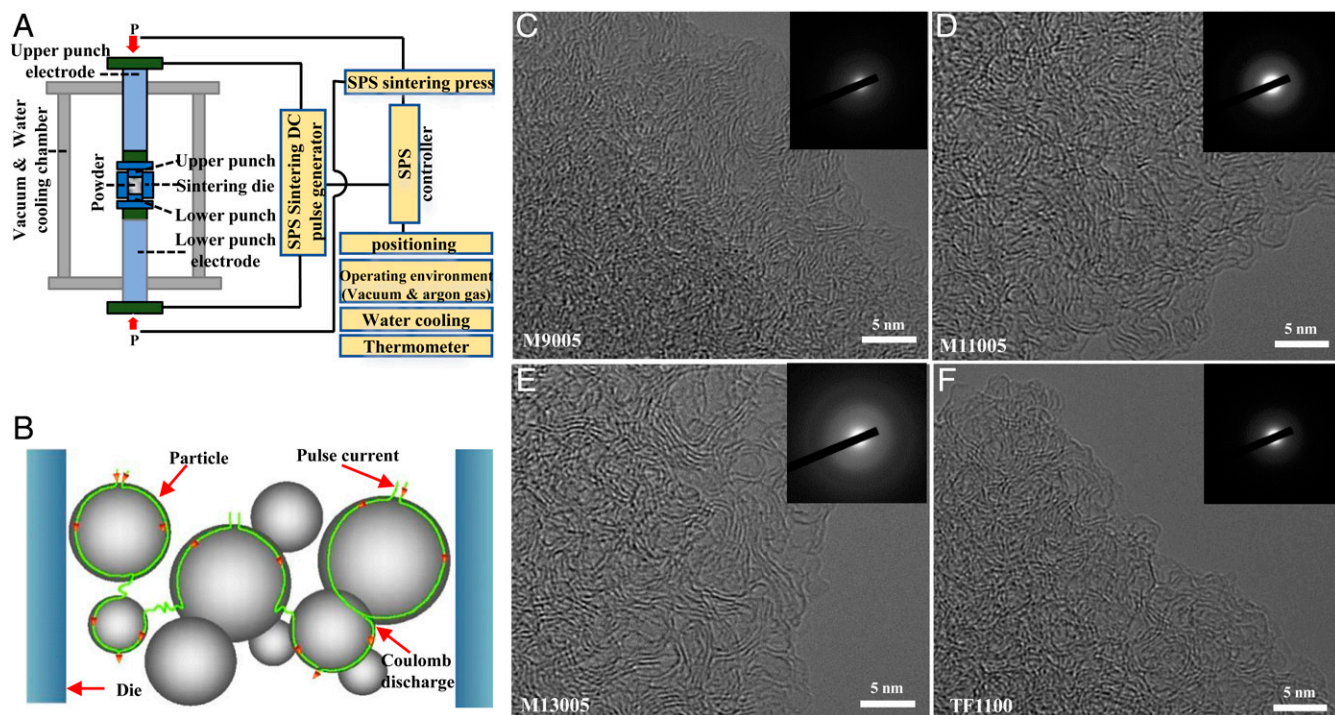
CHEMISTRY

Fig. 1. (*A*) Schematic diagram of the SPS system and (*B*) the annealing mechanism. HRTEM and SAED images of (*C*) M9005, (*D*) M11005, (*E*) M13005, and (*F*) TF1100.

Results and Discussion

Sucrose is used as a carbon source for the comparative study of HC fabricated from both the SPS technology and from the traditional sintering process. The X-ray diffraction (XRD) patterns of different sucrose-derived HCs (SHCs) from different pyrolysis temperatures and methods are displayed in *SI Appendix*, Fig. S1. HCs via SPS at 900, 1,100, and 1,300 °C with a moderate heating rate (300 °C min^{-1}) and 5 min sintering duration are denoted as M9005, M11005, and M13005, respectively. All the XRD patterns have two broad characteristic peaks near 23° and 43°, corresponding to the carbon crystal plane of (002) and (101). For the SHCs via the SPS, the (002) peak shifts to a higher angle with the increased pyrolysis temperature, suggesting a decreased averaged layer spacing. According to Bragg's law, the interlayer spacings (d_{002}) of M9005, M11005, and M13005 are calculated as 3.85, 3.83, and 3.73 Å, respectively. Whereas, the HC (TF1100) obtained from the traditional way has a larger layer spacing than M11005 (3.99 Å) at the same sintering temperature. Scanning electron microscope (SEM) images (*SI Appendix*, Fig. S2) show the morphology of SHC particles, indicating that the sintering temperature and method have a negligible effect on their morphology. High-resolution transmission electron microscopy (HRTEM) images show that SHCs possess curved short-range layers, as shown in Fig. 1 *C–F*. With the increasing pyrolysis temperature, the rearrangement of carbon atoms changes the structure of SHCs from disorder to localized order. More graphite-like microcrystals with fringed curved carbon layers were folded, and the merge of nanopores increased the number of closed nanopores and the formation of HC (11). Such pores can facilitate sodium storage based on the pore-filled model (13, 16, 21, 22, 30, 31). The corresponding selected area electron diffraction (SAED) pattern of SHCs is characterized by diluted spots to a recognizable polycrystalline ring, which indicates the formation of a localized ordered structure with an increase in pyrolysis temperature.

Comprehensive characterizations were conducted to investigate the detailed microstructure and the compositions of SHCs, as listed in Table 1. The open pores on the surface of SHCs can be measured by the nitrogen adsorption/desorption method instead of internal and closed micropores (Fig. 2*A*). The Brunauer–Emmett–Teller (BET) surface area of SHCs prepared by the SPS method decreased sharply from 279.5 to 9.2 m$^2 \cdot$g^{-1} and then to 3.2 m$^2 \cdot$g^{-1} from 900 to 1,100 °C and 1,300 °C with the reduction in defects and oxygen content. The surface area of all the HCs is mainly from micropores, as revealed from the Non-Local-Density Functional Theory (NLDFT) pore size distribution (Fig. 2*B*), while the pore volumes decreased from 0.108 cm$^3 \cdot$g^{-1} (900 °C) to 0.003 cm$^3 \cdot$g^{-1} (1,100 °C) and 0.001 cm$^3 \cdot$g^{-1} (1,300 °C). It is worth noting that the specific surface area and pore volume of the samples synthesized by SPS and traditional tubular furnaces are significantly different. TF1100 showed a much larger surface area (57.4 m$^2 \cdot$g^{-1}) and pore volume (0.022 cm$^3 \cdot$g^{-1}), indicating that the SPS is capable of quickly reducing the concentration of pores and defects. A small-angle X-ray scattering (SAXS) technique can effectively probe the presence and size of closed pores by fitting the characteristic length to scattering power variation (32). Fig. 2*C* shows the SAXS patterns of SHCs; both M11005 and TF1100 induce a plateau region around 0.1 Å^{-1}, which significantly distinguishes from commercial graphite of highly ordered and dense structure with negligible internal pores, indicating the formation of closed nanopores within SHCs. The average pore diameter of M11005 and TF1100

Table 1. Structure and composition information of SHCs

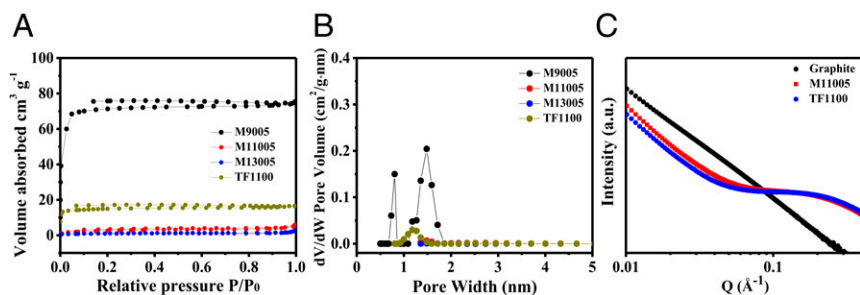| Sample	d_{002} (Å)	C (at%)	O (at%)	C/O	I_D/I_G	SBET (m$^2 \cdot$g^{-1})
M9005	3.85	95.09	4.91	19.37	3.42	279.5
M11005	3.83	95.98	4.02	23.88	3.00	9.2
M13005	3.73	96.54	3.46	27.90	2.52	3.2
TF1100	3.99	94.13	5.87	16.04	3.25	57.4

Fig. 2. (*A*) Nitrogen adsorption/desorption isotherms, (*B*) NLDFT pore size distribution, and (*C*) SAXS patterns of SHCs.

was calculated to be 1.91 and 1.76 nm, respectively, and the detailed fitting is demonstrated in *SI Appendix*, Fig. S3.

Raman spectroscopy was used to further evaluate the structure and defects of SHCs. Raman spectra have two characteristic bands, around 1,339 and 1,579 cm^{-1}, corresponding to defect structure (D band) and graphitic lattice (G band) within graphene layers, respectively (33). As shown in Fig. 3 *A–C* and Table 1, the integrated intensity ratio of I_D/I_G decreased from 3.42 to 3.00 as the heat treatment temperature increased from 900 to 1,100 °C and then decreased to 2.52 at 1,300 °C, indicating that the defect concentration decreased as the pyrolysis temperature increased. For traditional TF sintering (TF1100), the I_D/I_G is higher than that of M11005, suggesting a higher defect concentration. X-ray photoelectron spectroscopy (XPS) analysis (survey in *SI Appendix*, Fig. S4 and Table 1) for SHCs uncovers the atomic ratio of carbon to oxygen (C/O) increases gradually from

19.37 to 27.90 with the increase in temperature due to the reduction of sp^3 hybrid carbon at the defect sites of HC and carbon-oxygen linkages (34). The atomic ratio of C/O of TF1100 is 16.04, which is smaller than that of M11005 (C/O = 23.88), meaning traditional TF sintering results in a higher percentage of sp^3 hybrid carbon and carbon-oxygen polar bond, which is in good agreement with the Raman results above. The XPS spectra reveal the chemical bond configurations of carbon and oxygen. Firstly, as shown in Fig. 3 *D–F*, five separated peaks can be obtained for C 1s at 284.8, 285.3, 286.7, 288.4, and 290.7 eV, which can be assigned to triangular bonded carbon (sp^2), tetrahedral bonded carbon (sp^3), C-O bond, C = O bond and π-π*, respectively (34–36). Sp^2 hybridized carbon atoms form a honeycomb graphene layer while the sp^3 bonds are usually located at defect sites. The detailed composition of C 1s for the different samples (*SI Appendix*, Table S1) shows that the sp^2 carbon atoms
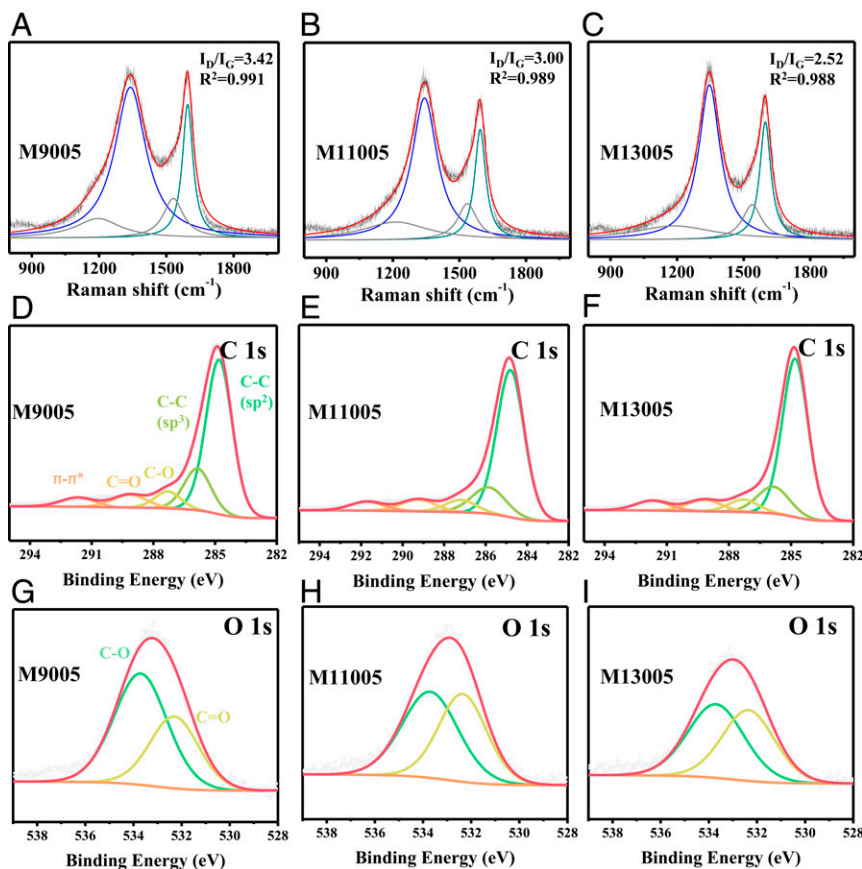

Fig. 3. (*A–C*) Fitted Raman spectra of SHCs with different temperatures based on the Lorentz function. The Raman spectra are divided into four bands (i.e., T-, D-, D′-, and G-bands) (from small to large Raman shift, respectively). R^2 is a coefficient of determination. The high-resolution XPS spectra for (*D–F*) C 1s and (*G–I*) O 1s of SHCs.

CHEMISTRY

gradually increase with the increase in pyrolysis temperature, while the relative content of the C-O bond and C = O bond decrease. These results reflect the reduction in the concentration of defects and oxygen atoms and the facilitated formation of carbon sp^2 structure, which coincides with Raman analysis. It should be noted that HC fabricated from SPS (63.13 at%) has fewer C-O groups than that from the traditional tubular furnace (43.30 at%) at the same pyrolysis temperature. Fig. 3 *G–I* show the high-resolution O 1s in SHC mainly from C-O at 533.4 eV and C = O at 532.1 eV (37–39). The proportion of C-O groups gradually decrease with the increase in temperature (*SI Appendix,* Table S2). As a result, the SPS technology effectively accelerates the pyrolysis process of HC materials with few defects, leading to a remarkably shortened pyrolysis time.

To study the rapid pyrolysis mechanism of the SPS process with multifield-regulated effect, large-scale molecular dynamics simulations were conducted. Three kinds of implemented simulative conditions with a constant temperature (1,100 °C) were built to illustrate the different annealing mechanism. One is without an external field, another one is under external pressure of 25 MPa only, and the last one is under applied bias (3.0 V/nm) and 25 MPa. The initially and finally obtained structures are shown in Fig. 4 *A–D*. It can be noticed that lots of individual carbon atoms were rapidly and epitaxially bonded to graphene layers under an external field. However, such behavior is relatively slow and applicable for few carbon atoms without an external field. A dilute system with randomly orienting graphene layers was kept during the whole carbonation process. By contrast, as shown in Fig. 4*D*, a relative compacted structure is obtained. This could be the reason why the as-prepared HC by the SPS process has smaller interlayer spacings and lower surface areas. The visual dynamic procedures for these two processes are listed in the *SI Appendix* (Movies S1 and S2),

showing a faster transport and reduction of isolated carbon atoms bonding to graphene sheets. In addition, as presented in Fig. 4*E*, the sp^2/sp^3 ratio during simulation for the three simulative conditions is quantified. To better understand the remarkable effect of electric field, final material under external pressure only was also simulated; the increase speed in sp^2/sp^3 ratio is lower than that under applied bias and external pressure but is a bit higher than that without any external field. In the case of the annealing process under applied bias and external pressure, the pyrolysis process is significantly accelerated from the high sp^2/sp^3 ratio, affirming the rapid formation of HC and low defect nature of the product from the SPS process. In order to investigate the effect of electric field on electronic distribution, density functional theory calculations were performed; the results are shown in *SI Appendix*, Fig. S5. The yellow region represents electron concentration (i.e., electro-negative region) while blue represents the electro-positive region. It can be seen on the edge of the graphene nano-flake that it had the most notable charge distribution change upon electric field, which may provide favorable sites for carbon to absorb. Recently, Tour et al. (26, 27) reported a work of bottom-up flash graphene synthesis also by Joule heating. They used a rapid power dissipation of ~30 kW in a very short time and produced a very high temperature of ~3,000 K, enabling a flash synthesis of few-layer graphene from various amorphous carbon resources. However, our power dissipation (<4 kW) and the target temperature are much lower as we aim to rapidly fabricate HCs with a large interlayer spacing and closed pores, ensuring an excellent Na-ion storage performance. The weaker Joule heating of SPS technology is now favorable for fabricating HC and controlling its structure compared with the overfast heating rate, but it is still much faster than the traditional way. In addition, the SPS technology may be not suitable for the rapid
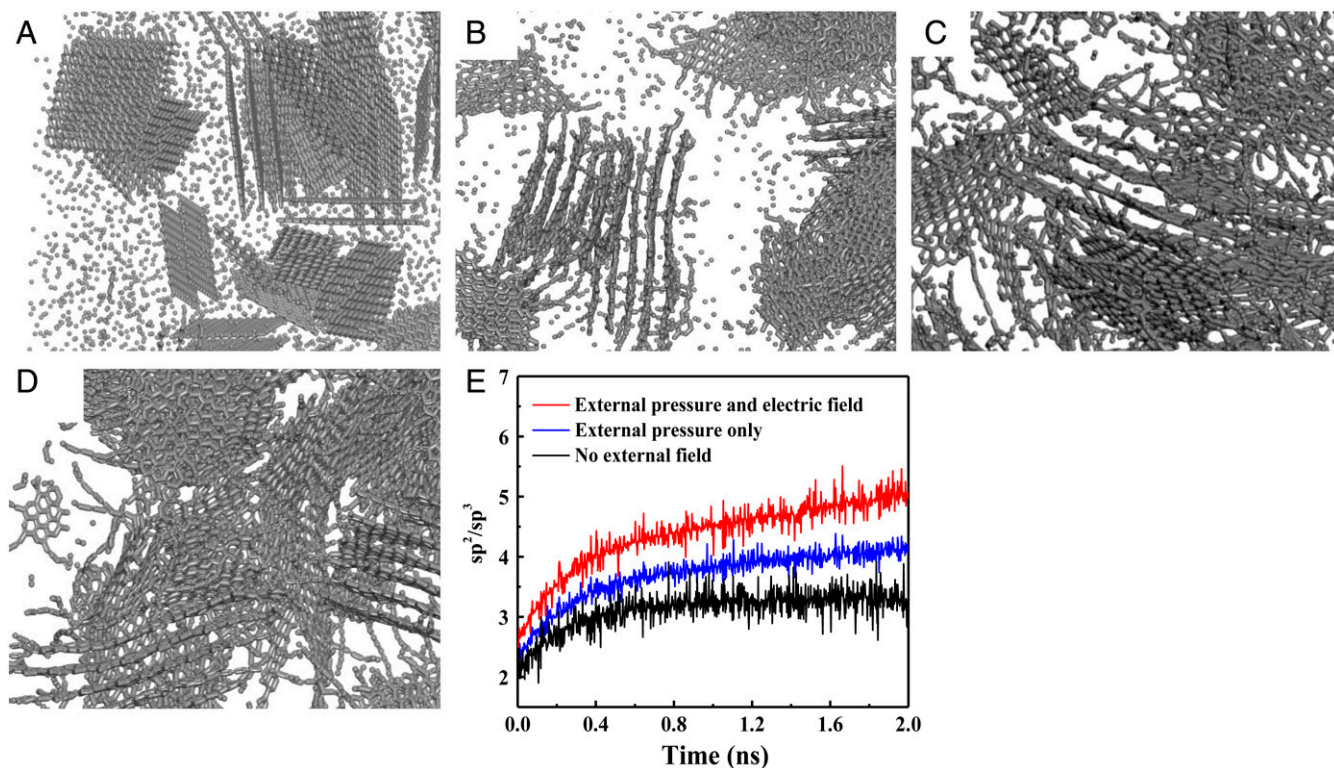

Fig. 4. Molecular dynamics simulations. (*A*) Initial structure. Final material held at the target temperature for 2×10^{-9} s (*B*) without external field, (*C*) under external pressure of 25 MPa only, and (*D*) under applied bias and external pressure of 25 MPa. (*E*) Change of the structural composition for materials under different conditions.
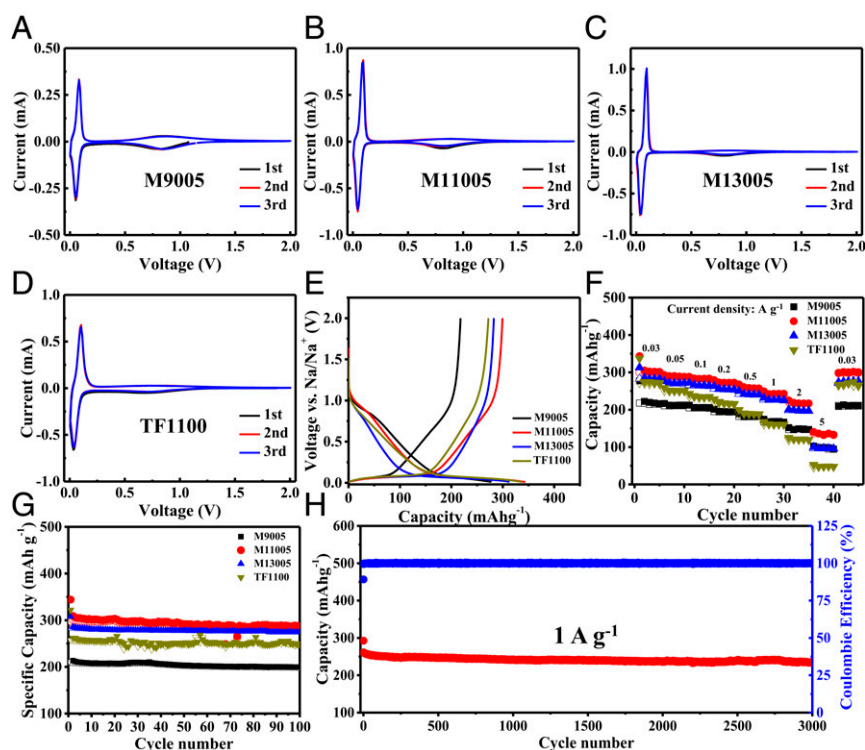
Fig. 5. (*A–D*) CV curves of SHCs at 0.1 mV·s^{-1} in a voltage range of 0.01 to 2 V. (*E*) Galvanostatic initial discharge/charge curves of SHCs at 0.03 A·g^{-1}. (*F*) Rate performance at enhanced current densities of the SHCs. (*G*) Cycling stability at constant 0.03 A·g^{-1} of SHCs. (*H*) A long cycle life test of M1105 at a high rate of 1 A·g^{-1}.

synthesis of graphene materials as the high-pressure condition (usually 15 to 80 MPa) makes the preferential formation of dense materials but is suitable for fabricating HC with smaller surface area and less porosity.

Na-ion half cells were assembled to demonstrate the applicability of SHCs anodes for SIBs. Cyclic voltammetry (CV) curves at 0.1 mV·s^{-1} for SHCs (Fig. 5 *A–D*) show a sharp peak near 0.1 V, and a broad peak appears in the voltage window of 0.5 to 1.5 V, corresponding to the plateau region and the sloping region (Fig. 5*E*) of a typical HC anode for SIBs, respectively. The peaks near 0.1 V turn sharper at a higher pyrolysis temperature, and the broad peak gradually weaken. Such a difference can be attributed to the less defect and lower porosity of HC from higher pyrolysis temperatures. The galvanostatic discharge/charge profiles of SHCs at 0.03 A·g^{-1} (Fig. 5*E*) can be divided into a sloping region above 0.1 V and a plateau region below 0.1 V. M9005 delivers a reversible capacity of 217.8 mAh·g^{-1} consisting of a short plateau capacity (80.1 mAh·g^{-1}) and a long sloping capacity (137.7 mAh·g^{-1}) with an initial Coulombic efficiency (ICE) of 80.1%. The irreversible capacity is largely associated with the initial formation of solid electrolyte interphase during the first few cycles (40). It is worth noting that M11005 displays a reversible capacity of 299.4 mAh·g^{-1} with a high ICE of 88.9% and an increased plateau capacity (152.5 mAh·g^{-1}). The increase in pyrolysis temperature change the contribution of reversible capacity such that M13005 delivered the highest platform capacity (170.0 mAh·g^{-1}) and the lowest slope capacity (112.6 mAh·g^{-1}), while the overall reversible capacity slightly decreases to 282.6 mAh·g^{-1}, but the ICE is as high as 91.2%. However, TF1100 has a lower reversible capacity (272.0 mAh g^{-1}) and ICE (80.6%) than that of M11005. The improved ICE confirms that HC with few defects and low porosity by a low heating rate (0.5 °C·min^{-1}) in a TF can reduce the irreversible capacity (24).

The rate performance of the SHCs electrode is presented in Fig. 5*F*. The reversible capacity of TF1100 electrode from 0.03 A·g^{-1} to 5 A·g^{-1} is 272.0, 250.7, 235.6, 220.3, 190.0, 161.3, 119.3, and 46.1 mAh·g^{-1}, respectively, which are similar to the performance of HC in ether-based electrolytes reported in previous literature (41). However, the HC electrode prepared via SPS has a better rate performance. M11005 delivers higher reversible capacities than M9005 and M13005 at different current densities; the corresponding capacities are 299.4, 288.5, 282.5, 272.5, 259.5, 242.4, 220.5, and 136.6 mAh·g^{-1}, respectively. When the current density returned to 0.03 A·g^{-1}, the reversible capacity was returned to similar values of the first five cycles for all the SHCs electrodes, indicating high reversibility and stability in a wide discharge-charge current range. Regarding the cycling performance (Fig. 5*G*), the reversible capacity of SHCs only slightly decreased at 0.03 A·g^{-1} after 100 cycles. High retention of 88% and 92% for M11005 and M13005 are obtained, respectively. Remarkably, a specific capacity of ∼250 mAh·g^{-1} was retained after 3,000 cycles at a high rate of 1 A·g^{-1} (Fig. 5*H*), indicating an outstanding long cycle life of the prepared HC anode. In addition, the Na$^+$ diffusion coefficient was calculated from the galvanostatic intermittent titration technique, as shown in *SI Appendix*, Fig. S6. The curves can be divided into two parts at the boundary of 0.1 V, corresponding to the slope and platform region in the discharge profile. M11005 displays a bit higher Na$^+$ diffusion coefficient than TF1100. In addition, the HC prepared by the SPS has better electrical conductivity than that from conventional TF. The measured conductivity of M11005 is 0.38 S·cm^{-1} at room temperature, which is higher than 0.16 S·cm^{-1} for TF1100. Another reason responsible for the improved performance is the remarkably lower oxygen content and porosity of HC from SPS, which can reduce the irreversible reactions enabling the higher ICE.

Zhen et al.
Ultrafast synthesis of hard carbon anodes for sodium-ion batteries

PNAS | 5 of 7
https://doi.org/10.1073/pnas.2111119118

CHEMISTRY

Besides, we also investigated the effects of sintering times and heating rates on the structure and properties of the materials, as shown in *SI Appendix*, Figs. S7 and S8. HC materials can be obtained even after calcination within one minute, which displays the same reversible capacity ($\sim$270 mAh·g^{-1}) as that from 10 min annealing. With the increase in calcination time, the d_{002} remain unchanged, but the defect concentration of the material decreases gradually from the Raman spectra. Optimized electrochemical properties are obtained when the HCs are calcined for five minutes. On the other hand, the heating rate by the SPS technology even at a fast rate of 500 °C·min^{-1} has a negligible impact on the Na-ion insertion properties. The three samples prepared at different heating rates display comparable performance. This result is different from the traditional annealing route, a very slow heating rate (0.5 °C·min^{-1}) is preferred to reduce the irreversible capacity coming from defects (24). This finding further verifies the applicability of the rapid synthesis strategy of HC anodes with high performance by the SPS process. To further confirm the applicability of the SPS fabricating HC materials, different carbon precursors, such as fructose, glucose, and phenolic resin (PH), were also sintered by this technology under the above-optimized conditions. The XRD patterns of all HCs from different precursors have two broad peaks around 23° and 43° (*SI Appendix*, Fig. S9). The d_{002} of fructose-derived HC (FHC), glucose-derived HC (GHC), and PH-derived HC (PHC) are 3.84, 3.79, and 3.80 Å, respectively. According to the SEM figure in *SI Appendix*, Fig. S10, four materials are all micron block materials. No matter what kind of precursors, SPS sintering technology can quickly and efficiently yield HC materials, which exhibit satisfied sodium storage capacity and rate capability. The galvanostatic discharge/charge curves and rate performance of HCs are shown in *SI Appendix*, Fig. S11. PHC delivers the highest reversible capacity of 312 mAh·g^{-1} among them. These results demonstrate a great universality of such a method in fabricating HC with good performance.

In summary, a field-assisted sintering process of the SPS method is firstly used to synthesize HCs from various carbon sources. This emerging technology cannot only prepare HC at a high rate of speed compared with traditional sintering routes but also effectively boost the pyrolysis process, leading to the formation of HCs with fewer defects and smaller surface areas.

Moreover, the accelerated pyrolysis mechanism is revealed by molecular dynamics simulations. As a result, HC made from the SPS method exhibits a significantly enhanced sodium storage capacity and kinetics. This study gives a high-efficiency and universal method to fabricate HC material with great promise in an industrial application.

Materials and Methods

Materials Synthesis. Firstly, sucrose (Aladdin) was used as raw material to prepare HC through SPS and the traditional way in a TF. Before the pyrolysis of sucrose, it was dehydrated by heat treatment in the air at 180 °C and formed into brown powdery precursors after ball milling. Then, the brown powder was put into a corundum boat and precarbonized in a TF filled with argon gas at 500 °C for 5 h. After the precarbonation, the black powder was ground and put into the SPS hot pressing sintering furnace at a moderate rate of 300 °C·min^{-1}, 3 V applied voltage, and 20 MPa pressure to different temperatures with a sintering time of 5 min (denoted as M9005, M11005, and M13005, respectively). The power dissipation is 3 to 4 kW with an output current of 300 to 600 A and a voltage of 3 to 6 V during the heating stage through the carbon precursor. The output power will change at a certain level depending on the different precursors. When arrived at the target temperature like 1,100 °C, the output power would decrease to around 1 kW with a smaller current and voltage around 3 V. After the instrument was cooled to room temperature, the block samples were taken out and ground to obtain black SHCs powder. After annealing at 1,100 °C for 1 and 10 min, SHCs are denoted as M11001 and M110010. Annealing at 1,100 °C for 5 min at a low heating rate of 100 °C·min^{-1} and fast rate of 500 °C·min^{-1}, the corresponding SHCs are denoted as L11005 and F11005, respectively. The dehydrated precursor was calcined in a TF at 1,100 °C for 3 h with a heating rate of 5 °C·min^{-1}, denoted as TF1100.

Besides, FHC and GHC were prepared in the same process way as sucrose by using fructose (Aladdin) and glucose (Aladdin) as carbon sources. PHC were fabricated by direct prepyrolysis of phenolic resin and then were ground for calcination by SPS without the dehydration process.

Data Availability. All study data are included in the article and/or supporting information.

1. N. Yabuuchi, K. Kubota, M. Dahbi, S. Komaba, Research development on sodium-ion batteries. *Chem. Rev.* **114**, 11636–11682 (2014).
2. C. Vaalma, D. Buchholz, M. Weil, S. Passerini, A cost and resource analysis of sodium-ion batteries. *Nat. Rev. Mater.* **3**, 18013–18024 (2018).
3. S.-W. Kim, D.-H. Seo, X. Ma, G. Ceder, K. Kang, Electrode materials for rechargeable sodium-ion batteries: Potential alternatives to current lithium-ion batteries. *Adv. Energy Mater.* **2**, 710–721 (2012).
4. V. Palomares *et al.*, Na-ion batteries, recent advances and present challenges to become low cost energy storage systems. *Energy Environ. Sci.* **5**, 5884–5901 (2012).
5. J.-Y. Hwang, S.-T. Myung, Y.-K. Sun, Sodium-ion batteries: Present and future. *Chem. Soc. Rev.* **46**, 3529–3614 (2017).
6. T. Liu *et al.*, Exploring competitive features of stationary sodium ion batteries for electrochemical energy storage. *Energy Environ. Sci.* **12**, 1512–1533 (2019).
7. K. Nobuhara, H. Nakayama, M. Nose, S. Nakanishi, H. Iba, First-principles study of alkali metal-graphite intercalation compounds. *J. Power Sources* **243**, 585–587 (2013).
8. Y. Okamoto, Density functional theory calculations of alkali metal (Li, Na, and K) graphite intercalation compounds. *J. Phys. Chem. C* **118**, 16–19 (2013).
9. Y. Li, Y. Lu, P. Adelhelm, M. M. Titirici, Y. S. Hu, Intercalation chemistry of graphite: Alkali metal ions and beyond. *Chem. Soc. Rev.* **48**, 4655–4687 (2019).
10. D. Saurel *et al.*, From charge storage mechanism to performance: A roadmap toward high specific energy sodium-ion batteries through carbon anode optimization. *Adv. Energy Mater.* **8**, 1703268–1703301 (2018).
11. X. Dou *et al.*, Hard carbons for sodium-ion batteries: Structure, analysis, sustainability, and electrochemistry. *Mater. Today* **23**, 87–104 (2019).
12. B. Xiao, T. Rojo, X. Li, Hard carbon as sodium-ion battery anodes: Progress and challenges. *ChemSusChem* **12**, 133–144 (2019).
13. H. Au *et al.*, A revised mechanistic model for sodium insertion in hard carbons. *Energy Environ. Sci.* **13**, 3469–3479 (2020).
14. K. Kubota *et al.*, Structural analysis of sucrose-derived hard carbon and correlation with the electrochemical properties for lithium, sodium, and potassium insertion. *Chem. Mater.* **32**, 2961–2977 (2020).
15. J. Ding *et al.*, Carbon nanosheet frameworks derived from peat moss as high performance sodium ion battery anodes. *ACS Nano* **7**, 11004–11015 (2013).
16. Y. Li, Y.-S. Hu, M.-M. Titirici, L. Chen, X. Huang, Hard carbon microtubes made from renewable cotton as high-performance anode material for sodium-ion batteries. *Adv. Energy Mater.* **6**, 1600468–1600668 (2016).
17. F. Xie *et al.*, Hard-soft carbon composite anodes with synergistic sodium storage performance. *Adv. Funct. Mater.* **29**, 1901072–1901081 (2019).
18. H.-l. Wang, Z.-q. Shi, J. Jin, C.-b. Chong, C.-y. Wang, Properties and sodium insertion behavior of phenolic resin-based hard carbon microspheres obtained by a hydrothermal method. *J. Electroanal. Chem. (Lausanne)* **755**, 87–91 (2015).
19. P. Adelhelm *et al.*, From lithium to sodium: Cell chemistry of room temperature sodium-air and sodium-sulfur batteries. *Beilstein J. Nanotechnol.* **6**, 1016–1055 (2015).
20. R. Väli, A. Jänes, T. Thomberg, E. Lust, D-glucose derived nanospheric hard carbon electrodes for room-temperature sodium-ion batteries. *J. Electrochem. Soc.* **163**, A1619–A1626 (2016).
21. Y. Li *et al.*, Regulating pore structure of hierarchical porous waste cork-derived hard carbon anode for enhanced Na storage performance. *Adv. Energy Mater.* **9**, 1902852–1902861 (2019).
22. Q. Meng *et al.*, Tuning the closed pore structure of hard carbons with the highest Na storage capacity. *ACS Energy Lett.* **4**, 2608–2612 (2019).
23. T. Chen *et al.*, Fast synthesis of carbon microspheres via a microwave-assisted reaction for sodium ion batteries. *J. Mater. Chem. A Mater. Energy Sustain.* **2**, 1263–1267 (2014).
24. L. Xiao *et al.*, Low-defect and low-porosity hard carbon with high coulombic efficiency and high capacity for practical sodium ion battery anode. *Adv. Energy Mater.* **8**, 1703238–1703245 (2018).

25. C. Wang *et al.*, A general method to synthesize and sinter bulk ceramics in seconds. *Science* **368**, 521–526 (2020).

26. D. X. Luong *et al.*, Gram-scale bottom-up flash graphene synthesis. *Nature* **577**, 647–651 (2020).

27. M. G. Stanford *et al.*, Flash graphene morphologies. *ACS Nano* **14**, 13691–13699 (2020).

28. M. Suarez *et al.*, Challenges and opportunities for spark plasma sintering: A key technology for a new generation of materials. BurcuErtug. *Sinter. Appl.* **13**, 320–328 (2013).

29. P. Cavaliere, *Spark Plasma Sintering of Materials* (Springer Nature Switzerland AG, Cham, 2019).

30. P. Bai *et al.*, Elucidation of the sodium-storage mechanism in hard carbons. *Adv. Energy Mater.* **8**, 1703217–1703226 (2018).

31. B. Zhang, C. M. Ghimbeu, C. Laberty, C. Vix-Guterl, J.-M. Tarascon, Correlation between microstructure and Na storage behavior in hard carbon. *Adv. Energy Mater.* **6**, 1501588–1501597 (2016).

32. D. A. Stevensa, J. R. Dahn, An In situ small-angle X-ray scattering study of sodium insertion into a nanoporous carbon anode material within an operating electrochemical cell. *J. Electrochem. Soc.* **147**, 4428–4431 (2000).

33. A. Sadezky, H. Muckenhuber, H. Grothe, R. Niessner, U. Pöschl, Raman microspectroscopy of soot and related carbonaceous materials: Spectral analysis and structural information. *Carbon* **43**, 1731–1742 (2005).

34. K. Wang *et al.*, Sodium storage in hard carbon with curved graphene platelets as the basic structural units. *J. Mater. Chem. A Mater. Energy Sustain.* **7**, 3327–3335 (2019).

35. C. Chen *et al.*, Nonignorable influence of oxygen in hard carbon for sodium ion storage. *ACS Sustain. Chem. & Eng.* **8**, 1497–1506 (2020).

36. R. R. Gaddam, N. A. Kumar, X. S. Zhao, Carbon nanoparticle-based three-dimensional binder-free anode for rechargeable alkali-ion batteries. *Mater. Today Energy* **8**, 29–36 (2018).

37. J. L. Xia *et al.*, Hard carbon nanosheets with uniform ultramicropores and accessible functional groups showing high realistic capacity and superior rate performance for sodium-ion storage. *Adv. Mater.* **32**, e2000447 (2020).

38. Y. Wang *et al.*, Rational design of high-performance sodium-ion battery anode by molecular engineering of coal tar pitch. *Chem. Eng. J.* **342**, 52–60 (2018).

39. C. Zhou *et al.*, The non-ignorable impact of surface oxygen groups on the electrochemical performance of N/O dual-doped carbon anodes for sodium ion batteries. *J. Electrochem. Soc.* **165**, A1447–A1454 (2018).

40. J. Song, B. Xiao, Y. Lin, K. Xu, X. Li, Interphases in sodium-ion batteries. *Adv. Energy Mater.* **8**, 1703082 (2018).

41. P. Bai *et al.*, Long cycle life and high rate sodium-ion chemistry for hard carbon anodes. *Energy Storage Mater.* **13**, 274–282 (2018).

CHEMISTRY